Original Research

Cine Magnetic Resonance Microscopy of the Rat Heart Using Cardiorespiratory-Synchronous Projection Reconstruction

Anja C.S. Brau,[1,2]* Laurence W. Hedlund,[2] and G. Allan Johnson[2]

Purpose: To tailor a cardiac magnetic resonance (MR) microscopy technique for the rat that combines improvements in pulse sequence design and physiologic control to acquire high-resolution images of cardiac structure and function.

Materials and Methods: Projection reconstruction (PR) was compared to conventional Cartesian techniques in point-spread function simulations and experimental studies to evaluate its artifact sensitivity. Female Sprague-Dawley rats were imaged at 2.0 T using PR with direct encoding of the free induction decay. Specialized physiologic support and monitoring equipment ensured consistency of biological motion and permitted synchronization of imaging with the cardiac and respiratory cycles.

Results: The reduced artifact sensitivity of PR offered improved delineation of cardiac and pulmonary structures. Ventilatory synchronization further increased the signal-to-noise ratio by reducing inter-view variability. High-quality short-axis and long-axis cine images of the rat heart were acquired with 10-msec temporal resolution and microscopic spatial resolution down to 175 μm × 175 μm × 1 mm.

Conclusion: Integrating careful biological control with an optimized pulse sequence significantly limits both the source and impact of image artifacts. This work represents a novel integration of techniques designed to support measurement of cardiac morphology and function in rodent models of cardiovascular disease.

Key Words: cardiac MRI; MR microscopy; projection reconstruction (PR); radial acquisition; small animal; gating
J. Magn. Reson. Imaging 2004;20:31–38.

THE STUDY OF SMALL ANIMAL MODELS of human cardiovascular disease is critical to our understanding of the origin, progression, and treatment of the disease—the leading cause of death in the U.S. (1) and a major cause of death worldwide (2). The rat has been the most widely studied animal model in cardiovascular research over the last decade because its relatively low cost, short gestation period, and moderate size make it suitable for a range of physiologic tests (3). Rat models of hypertension, heart failure, hypertrophy, and cardiotoxicity can readily be produced from a known lineage of disease, through surgical or pharmacological intervention, or more recently, via transgenic techniques (4–6). While the biochemical and molecular aberrations related to cardiovascular disease have been studied extensively in these animal models, thorough analysis of disease pathology also requires measuring changes at the whole organ level. Thus, the purpose of this work was to design a noninvasive imaging technique appropriate for in vivo characterization of gross cardiac structure and function in rat models of cardiovascular disease.

Whereas current clinical magnetic resonance imaging (MRI) techniques provide reliable structural and functional assessment of the human heart (7,8), the extension of cardiac MRI from humans to rodents presents a formidable challenge. The physiology of the small animal impacts the imaging process in a number of significant ways. Table 1 compares several key biological parameters in the human and rat (data compiled from Davies and Morris (9) and Li (10) and empirical observation). The most critical distinction for imaging purposes is body weight; at 250 g, the rat is 280 times smaller than a 70-kg human. Accordingly, the rat requires a 280-fold reduction in voxel volume to achieve the same relative anatomic resolution, e.g., scaling from voxel dimensions of 1 × 1 × 10 mm (10 mm^3) in humans down to 190 μm × 190 μm × 1 mm (~0.03 mm^3) in rodents—within the microscopic imaging regime. Furthermore, the rat heart rate at 300 bpm requires a fivefold increase in acquisition speed over the human heart rate at 60 bpm to capture the same relative phases of the cardiac cycle. No single technical innovation can meet this simultaneous demand for increased spatial and temporal resolution. Though dedicated small animal gradient coils with higher magnetic

[1]GE Healthcare, Applied Science Laboratory West, Menlo Park, California.
[2]Duke University Medical Center, Center for In Vivo Microscopy, Durham, North Carolina.
Contract grant sponsor: NIH/NCRR; Contract grant number: NIH NCRR P41 RR05959.
Presented in part at the 8th Annual Meeting of ISMRM, 2000.
All research was performed at the Center for In Vivo Microscopy, Duke University Medical Center, Box 3302, Durham, NC 27710.
*Address reprint requests to: A.C.S.B., GE Healthcare, Applied Science Lab (ASL) West, 333 Ravenswood Ave., Bldg. 307, Menlo Park, CA 94025. E-mail: Anja.Brau@med.ge.com
Received August 26, 2003; Accepted February 23, 2004.
DOI 10.1002/jmri.20089
Published online in Wiley InterScience (www.interscience.wiley.com).

Table 1
Comparison of Biological Parameters in the Human and Rat

	Human	Rat
Body weight (g)	70,000	250
Heart weight (g)	330	1
Heart diameter (mm)	100	15
Heart excursion (mm)	30	5
Heart rate (bpm)	60	300
R-R interval (ms)	1000	200
Blood volume (mL)	5200	13.5
Cardiac output (mL/minute)	5600	74
Aortic flow (cm/second)	23.2	16.6
Breathing rate (breaths/minute)	12	60
Tidal volume (mL)	500	3
Minute volume (L/minute)	6	0.18

field strengths and slew rates can technically meet the need for smaller voxels and faster acquisition speeds, they cannot compensate for the dramatic signal loss that accompanies finer sampling in space and time. Therefore, several methods must be integrated to improve system sensitivity and recover the signal-to-noise ratio (SNR), including the use of smaller-radius radio frequency (RF) coils, higher main magnetic field strengths, and extensive signal averaging.

Given sufficient improvement in SNR, however, the next practical impediment to spatial resolution in small animal cardiac imaging is motion of the heart and lungs. Although the mechanisms by which motion degrades MR image quality are well known, existing methods to reduce motion artifacts are only partly effective. Gradient moment nulling can be employed to reduce phase shifts caused by intra-view motion, but the additional gradient lobes prolong the echo time (TE), in turn increasing T_2* losses and susceptibility to higher-order motion. Imaging can be synchronized with the animal's cardiac and respiratory cycles using MR-compatible small animal monitoring and gating equipment to minimize inter-view motion artifacts. However, biological synchronization ensures inter-view consistency only to the extent that the frequency and path of motion remain constant throughout the scan. Moreover, triggered MR data acquisition introduces inter-view inconsistencies of its own due to variable longitudinal magnetization recovery between imaging intervals.

Another strategy to reduce motion artifact sensitivity is a judicious choice of k-space sampling trajectory. In this work, we have tailored a cardiac MR microscopy technique for the rat that employs projection reconstruction (PR) (also known as radial acquisition), a pulse sequence known to hold a number of intrinsic advantages over conventional Cartesian sampling methods. While other groups have reported excellent cardiac imaging results in the rat, all studies have been limited to Cartesian techniques, both the slower "black blood" spin echo sequences (11,12) and the faster "white blood" gradient echo sequences such as FLASH (fast low-angle shot) (13–15). By initiating data acquisition at the k-space origin, PR methods can encode the free induction decay (FID) directly, minimizing intra-view motion-dependent phase accrual and exhibiting decreased vulnerability to flow artifacts relative to Cartesian methods (16,17). Furthermore, Glover and Pauly (18) demonstrated that inter-view breathing motion artifacts are less conspicuous using PR, appearing as diffuse radial streaks at a distance from the subject rather than as coherent ghosts along the phase-encoding direction. Because PR has been shown to be robust to inter-view variation arising from motion, the technique should similarly prove tolerant of inter-view variation in the magnetization imposed by the gating process. This hypothesis was investigated and confirmed through point-spread function (PSF) simulations and imaging experiments. Other advantages of PR over Cartesian methods include inherent oversampling of low spatial frequencies and decreased T_2* losses due to shorter effective TE.

The PR method was combined with custom-built physiologic support equipment, including a pneumatic computer-controlled ventilator, a fiber-optic cardiac monitoring system, and an automatic temperature stabilization system, to mitigate both the source and impact of view-to-view instabilities during the imaging process. Respiratory-synchronous, cardiac-gated (termed cardiorespiratory-synchronous) PR images of the heart were acquired with 10-msec temporal resolution across the cardiac cycle and microscopic voxel dimensions down to 175 μm $\times$ 175 μm $\times$ 1 mm.

MATERIALS AND METHODS

PSF Simulation

Although the use of cardiorespiratory synchronization minimizes motion artifacts, it also introduces magnetization instabilities due to variable-length repetition time (TR) intervals during imaging (see Fig. 1). Dummy views or special preparatory pulses (19) can be applied to drive the system to a steady state and reduce the amount of inter-view variation; however, these techniques cost valuable imaging time during the rat's 200-msec cardiac cycle. To compare the tolerance of Cartesian vs. radial k-space sampling strategies to amplitude modulation caused by variable TR, their respective PSFs were calculated using MATLAB software (MathWorks, Natick, MA). The PSF simulation was modeled after Glover and Pauly's (18) work analyzing k-space sampling strategies in the presence of translational motion. The analytical k-space representation of a point source object was sampled using both Cartesian and radial trajectories. Successive k-space views were amplitude modulated with a periodic exponential decay function to mimic 10% magnetization variability observed in practice. The Cartesian k-space views were modulated along the phase-encoding direction, whereas the radial views were modulated along the azimuthal direction. The resulting PSF was then reconstructed from the k-space data to reveal the response of the system. To verify the PSF simulation results, a phantom was imaged using triggered Cartesian and radial sampling to assess the consequences of variable magnetization recovery on image quality. Use of a static phantom allowed us to isolate variable TR artifacts from motion artifacts. A trigger pulse was provided by an external gating source.

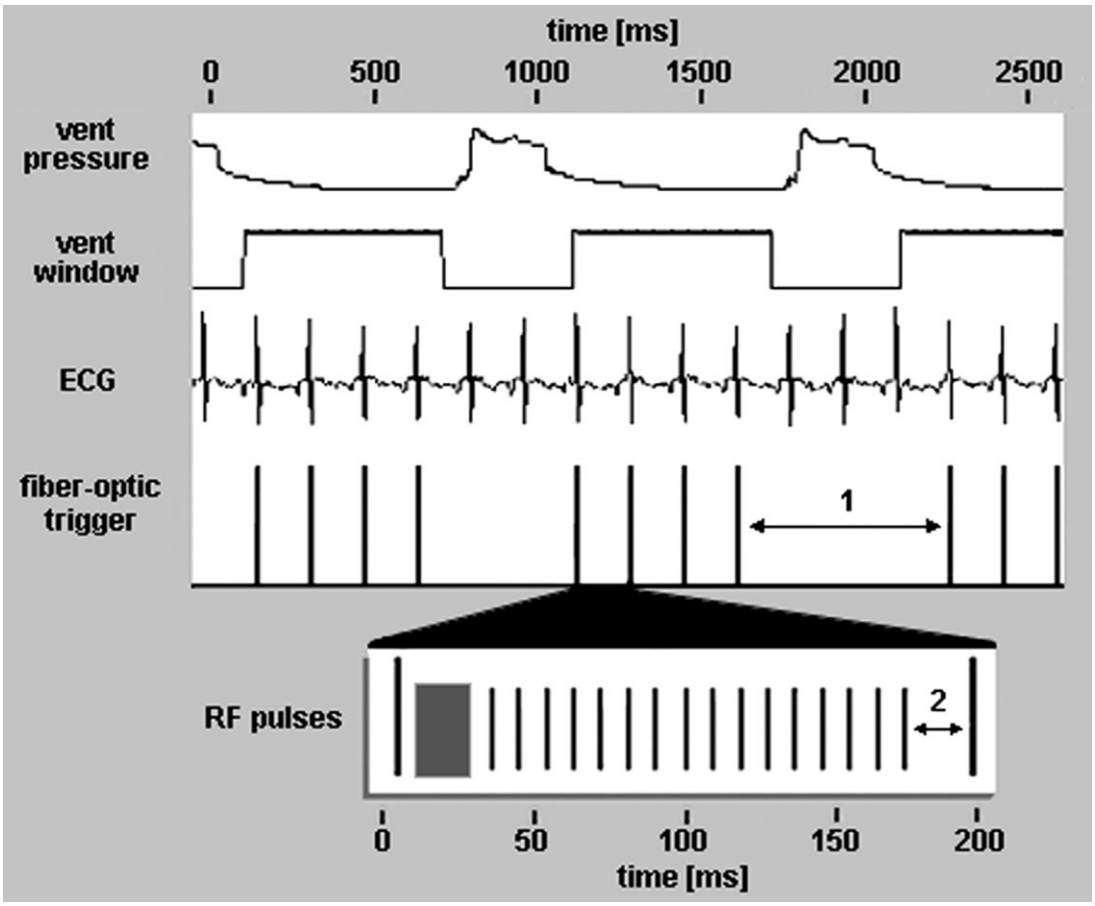

Figure 1. Representative physiologic and gating waveforms recorded over a 2.5-second period during a typical experiment, demonstrating the cardiorespiratory synchronization scheme. (Signals are arbitrarily offset and amplified for easier viewing.) Imaging was enabled by a 600-msec ventilatory window during end-expiration of the animal's breathing cycle. Cardiac-gated data acquisition was initiated by the detection of fiber-optic trigger pulses during this window; for an average heart rate of 300 bpm, three or four cardiac cycles per breath were detected. A single 200-msec cardiac cycle is expanded to show RF pulse application across the imaging interval. A ~20-msec preparatory pulse period (solid rectangle) is followed by data acquisition (vertical bars) spanning 90% of the baseline cardiac cycle. In this example, 16 views per cardiac cycle are acquired (TR = 10 msec), from which 16 separate cine images are reconstructed. The two double-sided arrows denote the intervals over which variable magnetization recovery can occur: 1) between successive ventilatory windows and 2) following data acquisition, prior to detection of the subsequent cardiac trigger pulse.

Animal Preparation

All animal procedures were approved by the Duke University Institutional Animal Care and Use Committee. Thirty adult female rats (Sprague-Dawley, Charles River, MA) weighing 220–310 g were imaged in this study. Representative results from five experiments are presented here. Rats were anesthetized with 45 mg/kg methohexital sodium (Brevital, Eli Lilly, Indianapolis, IN). Following intubation with a 16-gauge endotracheal catheter (Sherwood Medical, Tullamore, Ireland), anesthesia was maintained by 2–3% isoflurane (IsoFlo, Abbott Laboratories, North Chicago, IL) delivered by a computer-controlled, MR-compatible pneumatic ventilator (20). Ventilation parameters such as tidal volume, breathing rate, and relative duration of inhalation and exhalation were controlled by a custom LabVIEW application (National Instruments, Austin, TX) (18). For this study, the ventilator was adjusted to deliver a 3-mL tidal volume at a rate of 60 breaths/minute with an inhalation-to-exhalation ratio of 1:3. Airway pressure was measured by a solid-state pressure transducer on the breathing valve, while exhaled carbon dioxide (CO_2) was measured by a microcapnometer (Columbus Instruments, Columbus, OH) to monitor gas exchange.

A reference electrocardiograph (ECG) signal was acquired by taping electrodes (Blue Sensor, Medicotest, Denmark) to the animal's paws. However, due to voltage artifacts induced by rapid gradient switching during imaging, the R-wave of the ECG could not reliably be used as a cardiac gating trigger. Instead, a novel MR-compatible fiber-optic "stethoscope" was inserted into the animal's esophagus to detect cardiac activity optically rather than electrically, thereby making the measurement immune to electromagnetic interference. The details of this device have been described previously (21). Briefly, two optical fibers—one for transmitted and one for detected light—were bundled together and threaded ~6 cm down the esophagus to the mid-chest level. As light from the transmit fiber impinged upon the esophageal wall, the amount of reflected and scattered light detected by the second fiber varied over the cardiac cycle in response to mechanical cardiac contrac-

tion. A signal processing circuit then generated a trigger pulse coincident with the R-wave of the ECG that was used to measure heart rate and initiate cardiac-gated imaging. Exhaled CO_2, airway pressure, ECG, fiber-optic trigger, heart rate, and rectal temperature were continuously monitored and recorded during imaging using a custom LabVIEW application. Representative ventilatory and cardiac waveforms recorded during a typical experiment are shown in Fig. 1.

Imaging Setup

All imaging was performed on a 2.0-T, 30-cm-bore horizontal magnet (Oxford Instruments, Oxford, UK) with shielded gradients up to 200 mT/m and rise times of 200 μsec. The system is controlled by a Signa console (General Electric Healthcare, Waukesha, WI) running Revision 5.5 software. A 7-cm-diameter birdcage RF body coil was used for transmit and receive in all experiments. The anesthetized rat was placed prone on a Plexiglas cradle inside the coil and positioned in the magnet. Body temperature was maintained at 37± 0.1°C throughout the experiment by an automated feedback system that regulated heated airflow through the magnet bore (22). The combination of closely controlled body temperature and constant anesthesia delivery kept the animal's heart rate to within 10% of its baseline value throughout a typical study. Heart rate consistency during a cardiac-gated MR experiment is essential for accurate myocardial wall delineation and minimization of artifacts from variable TR (22).

Biological Synchronization

The cardiorespiratory synchronization scheme is depicted in Fig. 1. To limit motion artifacts from breathing, imaging was enabled by a 600-msec "ventilatory window" defined by the ventilator control software during end-expiration, the period of the breathing cycle when there is least motion and the lungs are at lowest volume. Cine data acquisition was prospectively triggered by the detection of optically derived cardiac gating pulses during the ventilatory window. For an average heart rate of 300 bpm, the width of the window was sufficient to capture three or four cardiac cycles per breath over the course of the scan. The ventilatory window was defined such that even if a cardiac trigger occurred at the end of the window, there was sufficient time remaining during end-expiration to gather data from the full cardiac cycle.

Immediately after detection of a fiber-optic trigger, preparatory or dummy pulses (indicated by the solid rectangle in Fig. 1) were applied for ~20 msec to reduce inter-view magnetization variability and diminish the so-called lightning effect (23). To obtain good T_1 contrast weighting between the blood and myocardium derived from the inflow of unsaturated blood into the imaging plane, a TR between 8 and 12 msec and a flip angle α between 30 and 45° were chosen, depending on heart rate and slice thickness. K-space segmentation was not practical given the constraints of the fast rodent heart rate; rather, a single k-space view per image per cardiac cycle was acquired to achieve maximum temporal resolution and smoothest depiction of cardiac function. To accommodate fluctuations in heart rate up to 10%, imaging parameters were prescribed such that RF pulse application spanned only 90% of the cardiac cycle. Thus, for a typical baseline cardiac cycle of 200 msec (as shown in the Fig. 1 inset), after the initial 20-msec preparatory phase, 16 views were acquired with a TR = 10 msec, from which 16 separate cine images were reconstructed.

MR Pulse Sequence

The PR pulse sequence used in this work is an extension of the technique originally developed for pulmonary microscopy applications (24,25), adapted for time-resolved cardiac imaging. Data acquisition of the FID was initiated immediately after slice-selective excitation to acquire the k-space origin in an effective TE of ~1 msec (for FID imaging, the effective TE is defined as the interval between the middle of the RF pulse and acquisition of the first point in the FID). The RF pulse width was 1 msec, and slice thickness varied between 1 and 2 mm. Nonuniformly spaced data acquired on the rising readout gradient ramp were interpolated to uniform samples during the reconstruction process. To minimize errors from gradient nonlinearities, the gradient rise time was defined to be 552 μsec. The readout bandwidth (BW) was 62.5 kHz, the field of view (FOV) was 50–60 mm, and 256 data points per excitation were acquired for a total sampling period of 2.048 msec.

To satisfy the Nyquist criterion, at least 800 radial k-space "spokes" or views spaced evenly over the angular extent (0, 2π) are required to reconstruct an alias-free 256^2 pixel image ($800 \approx 256\pi$). However, when multiple signal averages (NEX) are desired, it is more appropriate from an SNR perspective to acquire a greater number of unique k-space views than to acquire the original 800 views multiple times. Increasing the number of unique k-space views decreases the size of k-space holes, thereby reducing the noise variance of the sampling scheme (26). Thus, for an effective NEX = 4, 3200 unique readout angles per image were traced out by the gradients, with gradients amplitudes Gx and Gy varying with the cosine and sine of the readout angle, respectively. For long-axis imaging, the FOV and readout interval were doubled (without increasing scan time) to minimize aliasing artifacts from outside the FOV (27). Image reconstruction was performed offline on an external workstation (Silicon Graphics, Inc., Mountain View, CA). Data were weighted and regridded from polar to Cartesian coordinates (28) prior to application of the fast two-dimensional Fourier transformation (2DFT).

Cartesian images acquired for comparison were obtained with a conventional FLASH sequence using BW = 62.5 kHz, FOV = 50–60 mm, TE/TR = 3.0/10 msec, $\alpha = 30°$, slice thickness = 2 mm, and 256 × 256 pixels.

RESULTS

PSF Simulation

The results of the PSF simulation comparing Cartesian vs. radial sampling schemes in the presence of inter-view amplitude variation are shown in Fig. 2. Ideally,

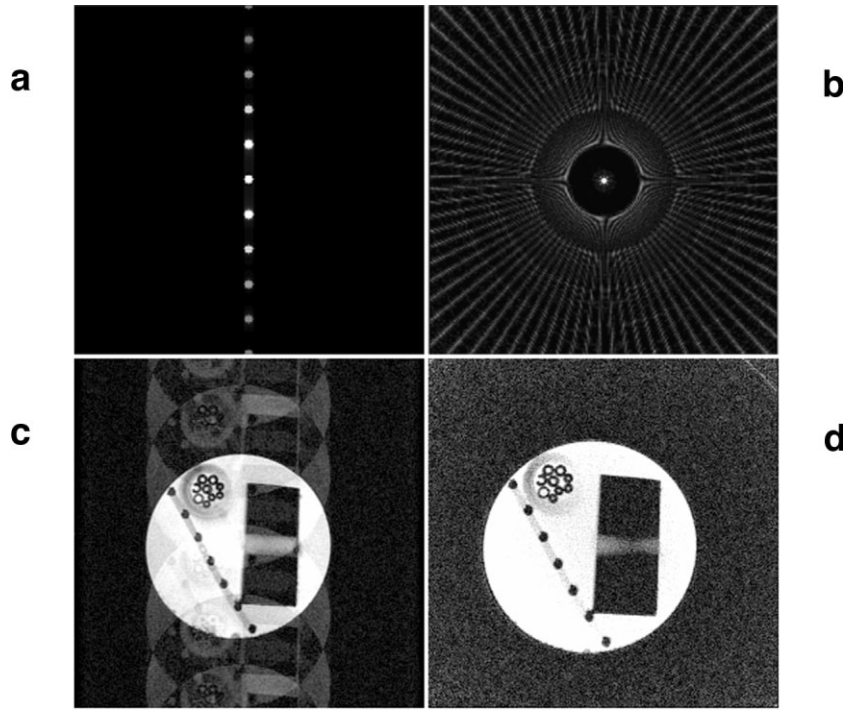

Figure 2. PSF comparison of Cartesian (**a**) vs. radial (**b**) sampling in the presence of inter-view amplitude variation, and triggered phantom images acquired with Cartesian (**c**) vs. radial (**d**) sampling. Images have been windowed to best display artifacts. a: The Cartesian PSF reveals discrete ghost artifacts along the phase-encoding (vertical) direction that tend to overlap and obscure the object of interest, as seen in the phantom image (c). b: The radial PSF distributes artifact energy as radial streaks throughout the image, resulting in less coherent structured noise in the reconstructed image and better visualization of structural detail (d).

the reconstructed image would reveal a single point source object centered at the origin. Instead, in Cartesian sampling (Fig. 2a), the point source at the center is accompanied by discrete ghost artifacts of varying intensity along the phase-encoding (vertical) direction. Convolution of this PSF with the object of interest would generate an image of the original object overlapped by low-intensity self-replicas. The triggered phantom image acquired with Cartesian sampling (Fig. 2c) confirms this result, with the phantom obscured by off-center ghost artifacts that misrepresent structural detail. The PSF simulation of radial sampling exhibits a very different pattern (Fig. 2b), with diffuse radial streaks emanating from the center point source rather than discrete, unidirectional ghosts. Accordingly, the radially sampled triggered phantom image (Fig. 2d) provides better visualization of object detail. The only evidence of artifact is the increased background noise resulting from more uniform dispersion of artifact energy throughout the image.

For simplicity, the PSF simulations and phantom experiments assumed perfect periodicity of amplitude modulation, resulting in the regularly spaced artifacts seen in Fig. 2. However, these results can be generalized to any condition that may arise in practice. Aperiodic amplitude fluctuations simply translate to more incoherent, smeared artifacts in the reconstructed image, although the character of artifact portrayal is preserved.

Just as the PR method was previously shown to be robust to motion artifacts (18), it is similarly shown here to be tolerant of variable TR artifacts. Together these results indicate that radial sampling is superior to Cartesian sampling for suppression of artifacts derived from any inter-view inconsistencies that occur during imaging.

In Vivo Experiments

An in vivo comparison of conventional gradient echo FLASH vs. PR imaging is shown in Fig. 3. The same animal was imaged with both sequences, and all imaging parameters were identical except TE, which was necessarily longer in FLASH to allow for prephasing gradient lobes. The total number of excitations was kept near constant by using 256 phase-encoding steps with NEX = 6 for the FLASH image and 1600 radial views for the PR image. Image acquisition was synchronized to both end-expiration of the ventilatory cycle and end-diastole of the cardiac cycle. Despite these efforts to mitigate the impact of motion, the gradient echo image (Fig. 3a) still exhibits significant ghost artifacts along the phase-encoding (horizontal) direction that obscure the anatomy of interest. Artifacts in this case stem not from bulk motion, but from pulsatile blood flow in the cardiac chambers and vessels. For example, a bright ghost of the vena cava appears in the far right lung (arrow) as a result of variable flow-induced phase shifts accrued during TE. In the PR image (Fig. 3b), blood signal homogeneity in the cardiac chambers and vessels is visibly improved due to better flow compensation. In addition, the delineation of myocardial wall borders is enhanced in the absence of ghost artifacts.

Figure 4 compares long-axis cardiac PR images of the same animal acquired without and with ventilatory synchronization. SNR is lower in Fig. 4a because, as demonstrated in the PSF simulations, inter-view variation in PR—derived in this case from inconsistent lung position—causes diffuse radial artifacts that increase the background noise level. Image quality increases when imaging is synchronized with breathing (Fig. 4b). Note the improved visualization of the brachiocephalic artery (top arrow) and the epicardial and diaphragmatic

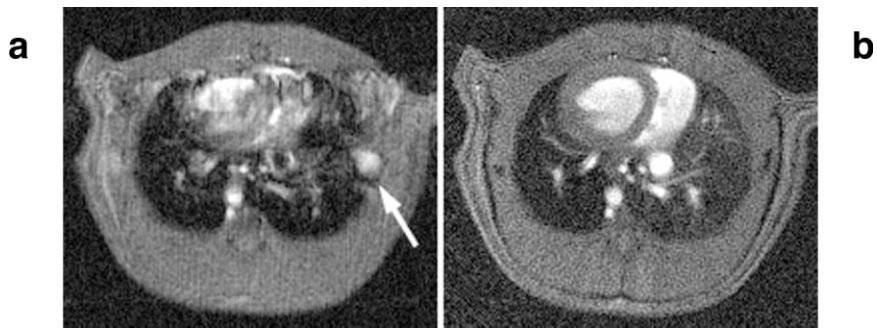

Figure 3. In vivo comparison of cardiorespiratory-synchronous FLASH (**a**) vs. PR (**b**) images acquired from the same animal. All imaging parameters were identical except TE, which was necessarily longer in the Cartesian case due to prephasing gradient lobes. a: Despite efforts to minimize motion, the Cartesian image exhibits significant ghosting artifacts along the phase-encoding (horizontal) direction stemming from blood flow in the cardiac chambers and vessels. A bright ghost artifact of the vena cava appears in the far right lung (arrow). b: The homogeneity of the blood signal in the cardiac chambers and vessels is improved due to the inherent flow compensation of the PR method, and the delineation of myocardial borders is easier in the absence of ghost artifacts.

borders (bottom arrow) due to consistent lung position during imaging. Note also the improved delineation of pulmonary tissue and vessels.

Representative cardiorespiratory-synchronous short-axis and long-axis cardiac PR images acquired during systole and diastole are shown in Fig. 5. Images were extracted from a cine series with imaging parameters of TE/TR = 1/10 msec, $\alpha = 30°$, views = 3200, scan time = 15 minutes, and spatial resolution = 195 μm $\times$ 195 μm $\times$ 2 mm. Changes in heart wall thickness and chamber size are evident as the heart cycles from the contraction phase (left column) to the filling phase (right column). In the long-axis images (bottom row), note that the aortic arch and associated branching arteries are clearly visualized during systole when unsaturated blood is ejected from the left ventricle into the aorta (Fig. 5c). However, after the aortic valve closes and the left ventricle begins filling during diastole, blood flow to the aortic arch temporarily ceases, resulting in poorer visualization of aortic structures (Fig. 5d).

Figure 6 shows a four-chamber view of the heart at four different phases of the cardiac cycle, demonstrating the ability of the technique to acquire high-resolution images of both structure and function. The images were acquired at 36, 72, 108, and 144 msec after the R-wave of the ECG. Imaging parameters were TE/TR = 1.4/12 msec, $\alpha = 40°$, views = 9600, scan time = 53 minutes, and spatial resolution = 175 μm $\times$ 175 μm $\times$ 1 mm. Slight radial streak artifacts are apparent during turbulent diastolic filling (Fig. 6c–d), but these artifacts do not significantly degrade image quality.

DISCUSSION

The results presented here emphasize two important points about small animal cardiac imaging. First, by carefully controlling and synchronizing biological motion, one can limit a primary source of image artifact. Temperature stabilization, mechanical ventilation, and cardiorespiratory synchronization serve to ensure consistency of physiologic motion and reduce inter-view variability during imaging. Although ventilatory synchronization prolongs scan time by roughly 40% (depending on ventilation parameters), it offers improved delineation not only of cardiac structures, but also of pulmonary tissue and vessels that constitute a critical component of the cardiovascular system. Second, by choosing an appropriate k-space sampling trajectory,

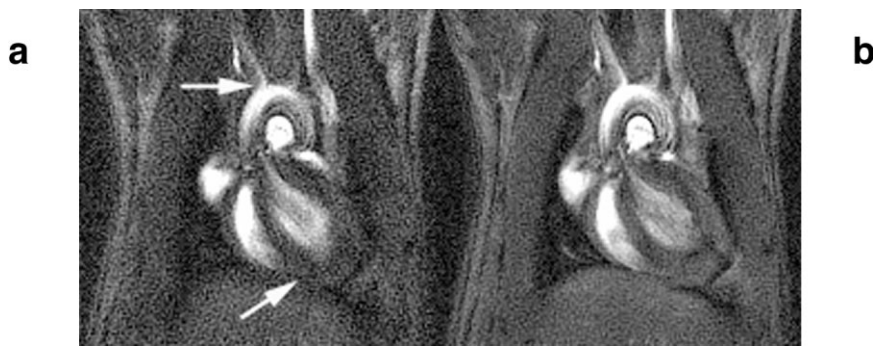

Figure 4. Long-axis cardiac PR images of the same animal acquired without (**a**) and with (**b**) ventilatory synchronization. a: The non-ventilatory-synchronous image is noisier and more blurry due to inconsistent lung position during imaging, which disperses artifact energy throughout the image and increases the background noise level. b: Synchronizing imaging with ventilatory motion reduces the amount of inter-view variation, thereby increasing SNR. Note the improved visualization of the brachiocephalic artery (top arrow) and cardiac and diaphragmatic borders (bottom arrow) due to consistent lung position during imaging.

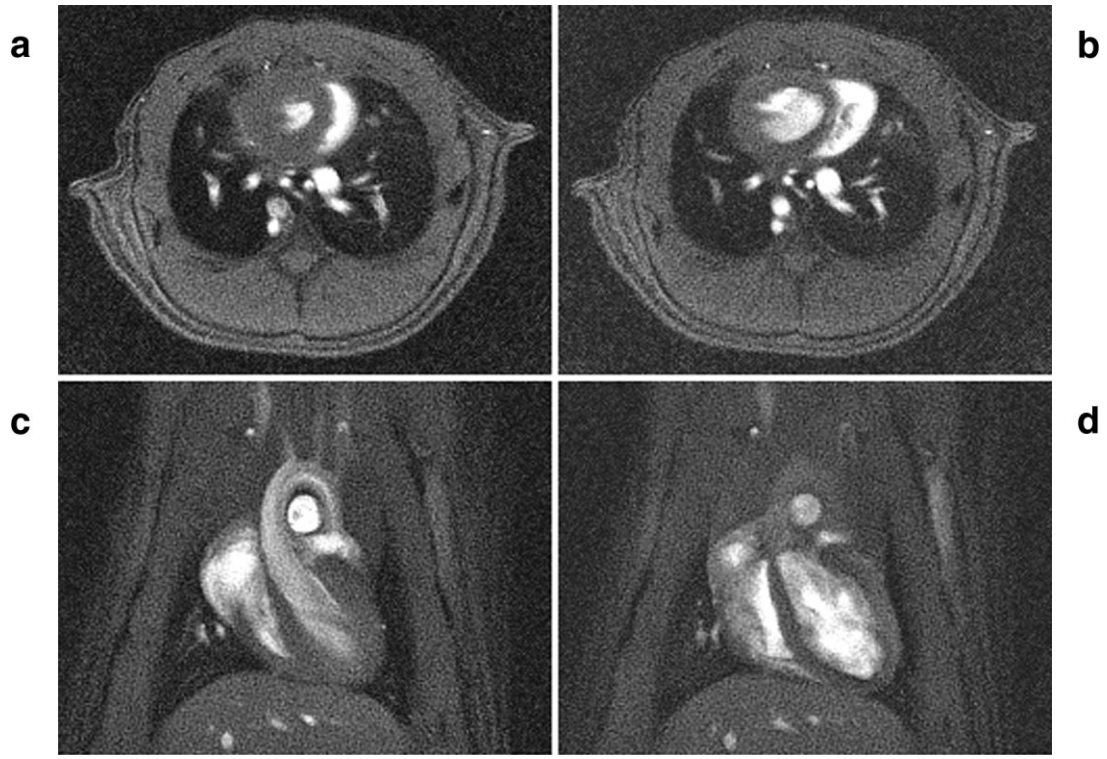

Figure 5. Cardiorespiratory-synchronous short-axis (**a,b**) and long-axis (**c,d**) PR images acquired during 10-msec intervals in systole (left column) and diastole (right column). Note the changes in heart wall thickness and chamber area as the heart cycles from the contraction phase to the filling phase. Due to inflow of unsaturated blood, the aortic arch appears bright during systole (c) and dark during diastole (d) after the aortic valve closes and blood flow to the aorta ceases.

one can reduce the impact of artifacts on image quality. The PR technique provides diminished sensitivity to inter-view and intra-view motion, as well as to gating-imposed magnetization inconsistencies. Together these techniques enable the acquisition of high-quality images of cardiac structure and function with minimal artifacts and markedly higher spatial resolution.

The PR method has a few potential disadvantages. A fully sampled PR image requires π times as many views as an equivalent Cartesian image, increasing total scan

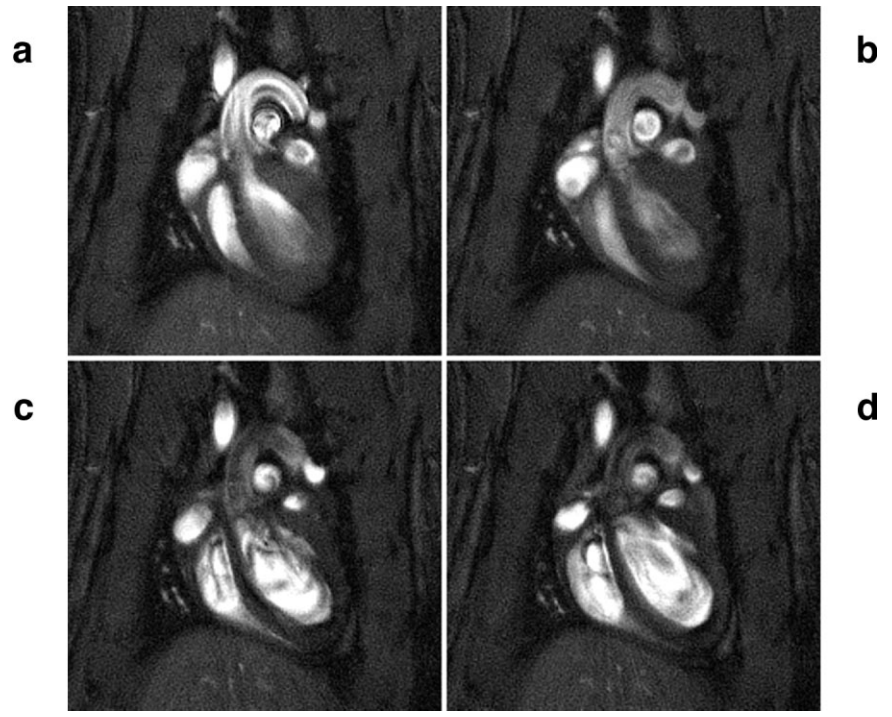

Figure 6. High-resolution four-chamber view of the rat heart in four phases of cardiac contraction, acquired (**a**) 36, (**b**) 72, (**c**) 108, and (**d**) 144 msec after the cardiac trigger. Dynamic changes in both ventricular and atrial chamber size are visible over the cardiac cycle. Imaging parameters were TE/TR = 1.2/12 msec, α = 40°, views = 9600, scan time = 53 minutes, and spatial resolution = 175 μm × 175 μm × 1 mm.

time. But this scan time penalty is not a significant drawback because extensive signal averaging is typically necessary in small animal imaging regardless of technique. Another possible limitation to radial sampling is that, all parameters being equal, it has inherently lower SNR than Cartesian sampling owing to its nonuniform sampling density (29). However, the benefit of artifact suppression and improved image quality offered by PR easily outweighs this disadvantage. In addition, off-resonance effects in PR are manifested as radial blurring rather than as a spatial shift, as in Cartesian imaging, but with a wide readout BW of 62.5 kHz, these effects were not significant. Finally, radially sampled images require an extra postprocessing step because the data must first be regridded prior to application of the 2DFT, but given the cost and speed of modern computers, this extra computational step is trivial.

Possible improvements to the technique presented here include the use of continuous RF application across the cardiac cycle. While this option was not available on our system, newer systems equipped with this ability should eliminate artifacts from variable magnetization recovery between TR intervals. Even with continuous RF application, however, inter-view inconsistencies will arise during in vivo imaging from motion, flow, and heart rate variability, compelling the need for a pulse sequence that tolerates these inconsistencies well. Another possible improvement is the incorporation of a self-refocused RF pulse, which would minimize TE and reduce flow artifacts by eliminating the slice-select rephasing lobe.

While the rat remains the most widely studied small animal model for cardiovascular research, recent advances in transgenic technology targeted at the mouse genome have created an abundance of mouse models whose genes have been modified to elicit a particular cardiovascular phenotype. Work is currently under way to extend the cardiorespiratory-synchronous PR imaging technique to the study of transgenic mouse models of cardiovascular disease.

ACKNOWLEDGMENTS

The authors thank Charles T. Wheeler for animal support and Sally Zimney for editorial assistance. This work was performed at the Duke Center for In Vivo Microscopy, an NIH/NCRR National Resource NIH NORR P41 RR05959.

REFERENCES

1. Minino A, Smith B. Deaths: preliminary data for 2000. National vital statistics Reports, Vol. 49, No. 12. Hyattsville, MD: National Center for Health Statistics; 2001.
2. World Health Organization. World health report. Geneva, Switzerland: World Health Organization; 2001.
3. Hasenfuss G. Animal models of human cardiovascular disease, heart failure and hypertrophy. Cardiovasc Res 1998;39:60–76.
4. Doggrell SA, Brown L. Rat models of hypertension, cardiac hypertrophy and failure. Cardiovasc Res 1998;39:89–105.
5. Pinto YM, Paul M, Ganten D. Lessons from rat models of hypertension: from Goldblatt to genetic engineering. Cardiovasc Res 1998; 39:77–88.
6. Herman EH, Zhang J, Chadwick DP, Ferrans VJ. Comparison of the protective effects of amifostine and dexrazoxane against the toxicity of doxorubicin in spontaneously hypertensive rats. Cancer Chemother Pharmacol 2000;45:329–334.
7. Cranney GB, Lotan CS, Dean L, Baxley W, Bouchard A, Pohost GM. Left ventricular volume measurement using cardiac axis nuclear magnetic resonance imaging. Validation by calibrated ventricular angiography. Circulation 1990;82:154–163.
8. Semelka RC, Tomei E, Wagner S, et al. Interstudy reproducibility of dimensional and functional measurements between cine magnetic resonance studies in the morphologically abnormal left ventricle. Am Heart J 1990;119:1367–1373.
9. Davies B, Morris T. Physiologic parameters in laboratory animals and humans. Pharm Res 1993;10:1093–1095.
10. Li JK-J. Comparative cardiovascular dynamics of mammals. Boca Raton, FL: CRC Press; 1996.
11. Manning WJ, Wei JY, Fossel ET, Burstein D. Measurement of left ventricular mass in rats using electrocardiogram-gated magnetic resonance imaging. Am J Physiol 1990;258:H1181–H1186.
12. Barone FC, Coatney RW, Chandra S, et al. Eprosartan reduces cardiac hypertrophy, protects heart and kidney, and prevents early mortality in severely hypertensive stroke-prone rats. Cardiovasc Res 2001;50:525–537.
13. Rehwald WG, Reeder SB, McVeigh ER, Judd RM. Techniques for high-speed cardiac magnetic resonance imaging in rats and rabbits. Magn Reson Med 1997;37:124–130.
14. Wise RG, Huang CL, Gresham GA, Al-Shafei AI, Carpenter TA, Hall LD. Magnetic resonance imaging analysis of left ventricular function in normal and spontaneously hypertensive rats. J Physiol 1998;513:873–887.
15. Nahrendorf M, Wiesmann F, Hiller KH, et al. Serial cine-magnetic resonance imaging of left ventricular remodeling after myocardial infarction in rats. J Magn Reson Imaging 2001;14:547–555.
16. Nishimura DG, Jackson JI, Pauly JM. On the nature and reduction of the displacement artifact in flow images. Magn Reson Med 1991; 22:481–492.
17. Jackson JI, Nishimura DG, Macovski A. Twisting radial lines with application to robust magnetic resonance imaging of irregular flow. Magn Reson Med 1992;25:128–139.
18. Glover G, Pauly J. Projection reconstruction techniques for reduction of motion effects in MRI. Magn Reson Med 1992;28:275–289.
19. Busse RF, Riederer SJ. Steady-state preparation for spoiled gradient echo imaging. Magn Reson Med 2001;45:653–661.
20. Hedlund LW, Johnson GA. Mechanical ventilation for imaging the small animal. ILAR J 2002;43:159–174.
21. Brau ACS, Wheeler CT, Hedlund LW, Johnson GA. The fiber optic stethoscope: a cardiac monitoring and gating system for magnetic resonance microscopy. Magn Reson Med 2002;47:314–321.
22. Qiu H, Cofer GP, Hedlund LW, Johnson GA. Automated feedback control of body temperature for small animal studies with MR microscopy. IEEE Trans Biomed Eng 1997;44:1107–1113.
23. Lenz GW, Haacke EM, White RD. Retrospective cardiac gating: a review of technical aspects and future directions. Magn Reson Imaging 1989;7:445–455.
24. Gewalt SL, Glover GH, MacFall JR, Hedlund LW, Johnson GA. MR microscopy of the rat lung using projection reconstruction. Magn Reson Med 1993;29:99–106.
25. Viallon M, Cofer GP, Suddarth SA, et al. Functional MR microscopy of the lung using hyperpolarized 3He. Magn Reson Med 1999;41: 787–792.
26. King KF. Spiral scanning with anisotropic field of view. Magn Reson Med 1998;39:448–456.
27. Song H. A simple technique for reducing aliasing artifacts in projection reconstruction MRI. In: Proceedings of the 9th Annual Meeting of ISMRM, Glasgow, Scotland, 2001. p 739.
28. Jackson J, Meyer C, Nishimura D, Macovski A. Selection of a convolution function for Fourier inversion using gridding. IEEE Trans Med Imaging 1991;10:473–478.
29. Lauzon ML, Rutt BK. Effects of polar sampling in k-space. Magn Reson Med 1996;36:940–949.